

# Chromospheric and coronal heating in an active region plage by dissipation of currents from braiding

Received: 8 February 2023

Accepted: 7 March 2024

Published online: 15 April 2024

 Check for updates

Souvik Bose<sup>1,2,3,4</sup>✉, Bart De Pontieu<sup>1,3,4</sup>, Viggo Hansteen<sup>1,2,3,4</sup>,  
Alberto Sainz Dalda<sup>1,2</sup>, Sabrina Savage<sup>5</sup> & Amy Winebarger<sup>5</sup>

The question of what heats the outer solar atmosphere remains one of the longstanding mysteries in astrophysics. Statistical studies of Sun-like stars reveal a correlation between global chromospheric and coronal emissions, constraining theoretical models of potential heating mechanisms. However, spatially resolved observations of the Sun have surprisingly failed to show a similar correlation on small spatial scales. Here we use unique coordinated observations of the chromosphere (from the IRIS satellite) and the low corona (from the Hi-C 2.1 sounding rocket), and machine-learning-based inversion techniques, to show a strong correlation on spatial scales of a few hundred kilometres between heating in the chromosphere and emission in the upper transition region in strong magnetic field regions ('plage'). Our observations are compatible with an advanced three-dimensional magnetohydrodynamic simulation in which the dissipation of current sheets caused by magnetic field braiding is responsible for heating the plasma simultaneously to chromospheric and coronal temperatures. Our results provide deep insight into the nature of the heating mechanism in solar active regions.

It has long been known from statistical studies of a wide variety of stars that the chromospheric and coronal emission are well correlated on a global, stellar scale<sup>1–3</sup>, which suggests that the heating mechanisms in the chromosphere and corona are related. This intriguing correlation potentially provides critical constraints on the heating mechanism responsible for non-thermal energy dissipation in a stellar atmosphere. This is because the chromosphere and corona are very different in terms of partial ionization, non-local thermodynamic equilibrium (non-LTE), stratification and magnetic field to plasma pressure ratio. These differences have varying effects on the efficiency and likelihood of different heating mechanisms.

The global correlations, however, have not been translated into a direct physical connection at high spatial and temporal scales in the solar atmosphere<sup>4–6</sup>, leaving potential heating mechanisms poorly constrained. Detailed correlation studies on small spatial scales

between coronal and chromospheric heating are very challenging because thermal conduction in the corona efficiently redistributes heat over a wide range of heights and locations. De Pontieu et al.<sup>4,5</sup> studied the correlation between heating sites in 'moss'—dynamic, bright regions of enhanced emission observed in the upper transition region (TR)/lower corona at the footpoints of high-pressure and high-temperature loops above an active region (AR) plage<sup>7</sup>, and the underlying chromospheric emission (visible in Ca H 3,968 Å filter images from ground-based telescopes). They found no correlation on arcsecond (~700 km) scales, in puzzling contrast with the global, stellar studies. These earlier studies were flawed, however, because recent results indicate that the bright 'chromospheric' emission in broadband Ca H 3,968 Å filter images is not a likely signature of chromospheric heating but rather emanates from deeper, hotter layers in the convection zone below evacuated strong photospheric

<sup>1</sup>Lockheed Martin Solar and Astrophysics Laboratory, Palo Alto, CA, USA. <sup>2</sup>Bay Area Environmental Research Institute, NASA Research Park, Moffett Field, CA, USA. <sup>3</sup>Institute of Theoretical Astrophysics, University of Oslo, Oslo, Norway. <sup>4</sup>Roseland Centre for Solar Physics, University of Oslo, Oslo, Norway.

<sup>5</sup>NASA Marshall Space Flight Center, Huntsville, AL, USA. ✉e-mail: [bose@lmsal.com](mailto:bose@lmsal.com)

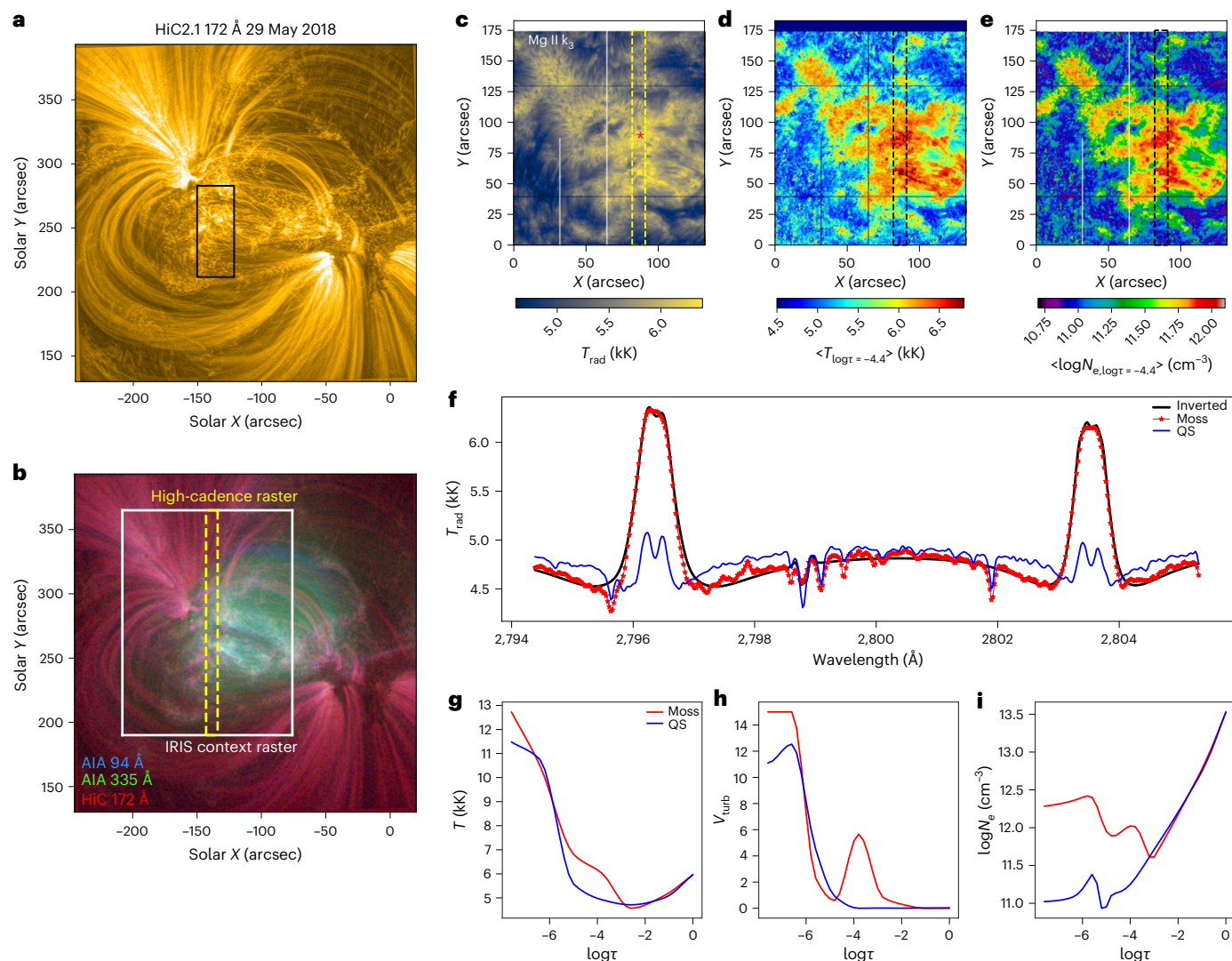


**Fig. 1 | The chromospheric and coronal scenery of the moss observed with Hi-C 2.1 and IRIS on 29 May 2018.** **a**, Hi-C 172 Å observation of AR 12712 centred at solar  $(X, Y) = (-145^\circ, 280^\circ)$ . The black rectangular box outlines the moss region studied in this paper. **b**, A composite layering showing Fe IX/x Hi-C 172 Å (red, 1 MK), Fe XVI 335 Å (green, 2.5 MK) and Fe XVIII 94 Å (blue, 6 MK) images from AIA. The white and dashed yellow boxes indicate the FOV recorded in the IRIS context and high-cadence rasters, respectively. **c**, The Mg II  $k_3$  emission ( $T_{\text{rad}}$ ) from the FOV of the context raster, with its origin shifted. **d, e**, The chromospheric

plasma temperature ( $T$ ) (**d**) and electron density ( $N_e$ ) (**e**) maps corresponding to the context raster averaged between  $\log\tau = [-4.6, -4.2]$ . The FOV of the high-cadence raster is outlined in **c–e, f**. The observed (red) and inverted (black) Mg II h&k profiles as a function of the wavelength corresponding to a moss pixel indicated in **c**. A typical QS profile is shown (blue) for reference. **g–i**, The stratification of  $T$  (**g**), microturbulent velocity (**h**) and  $N_e$  (**i**) of the moss (red) and QS (blue) inferred from IRIS<sup>2</sup> inversion.

magnetic flux tubes<sup>8,9</sup>. Upper TR moss provides an excellent laboratory to study how chromospheric and coronal heating mechanisms are spatio-temporally correlated. Because moss is formed in a thin layer, it is also very sensitive to changes in the local heating rate and avoids the confusion introduced by line-of-sight superposition that affects optically thin coronal diagnostics<sup>5,10</sup>. Most current observations lack the spatial resolution to resolve moss, which is structured on spatial scales of a few hundred kilometres. Recent observations from High-Resolution Coronal Imager (Hi-C) flight 1 (ref. 11) and the later Interface Region Imaging Spectrograph (IRIS<sup>12</sup>) satellite showed evidence of highly localized, small-scale, heating events in AR moss with durations between 15 s and 50 s (refs. 13,14). This relatively rare short-term, rapid variability is thought to be caused by the impact of non-thermal electrons, generated in the corona by reconnection in nanoflares<sup>15</sup>, on the upper TR and lower-lying chromosphere. While these observations hint at a relationship between chromospheric and coronal heating on small scales, these rare events do not seem to be

common enough to explain the relatively steady emission patterns in the low atmosphere.

In this Article, we use unique coordinated observations of AR moss at unprecedented high spatial and temporal resolution from IRIS and Hi-C sounding rocket flight 2.1 (ref. 16) to investigate the relationship between chromospheric and upper TR/low coronal heating on small spatial scales. We exploit recent advances in modelling of non-LTE radiative transfer of spectral lines formed in the chromosphere<sup>6,17</sup> that indicate that the enhancements in the cores of the chromospheric Mg II h&k lines in moss are well-defined signatures of chromospheric heating, in contrast to broadband Ca II H filter images. The combination of state-of-the-art spectral inversions of such lines with the high spatio-temporal resolution of the 5-min timeseries of Hi-C 2.1 images and numerical modelling allows us to determine unequivocally whether chromospheric and upper TR/low coronal heating are spatially and temporally correlated on small spatial scales, thereby providing strict constraints for numerical models.

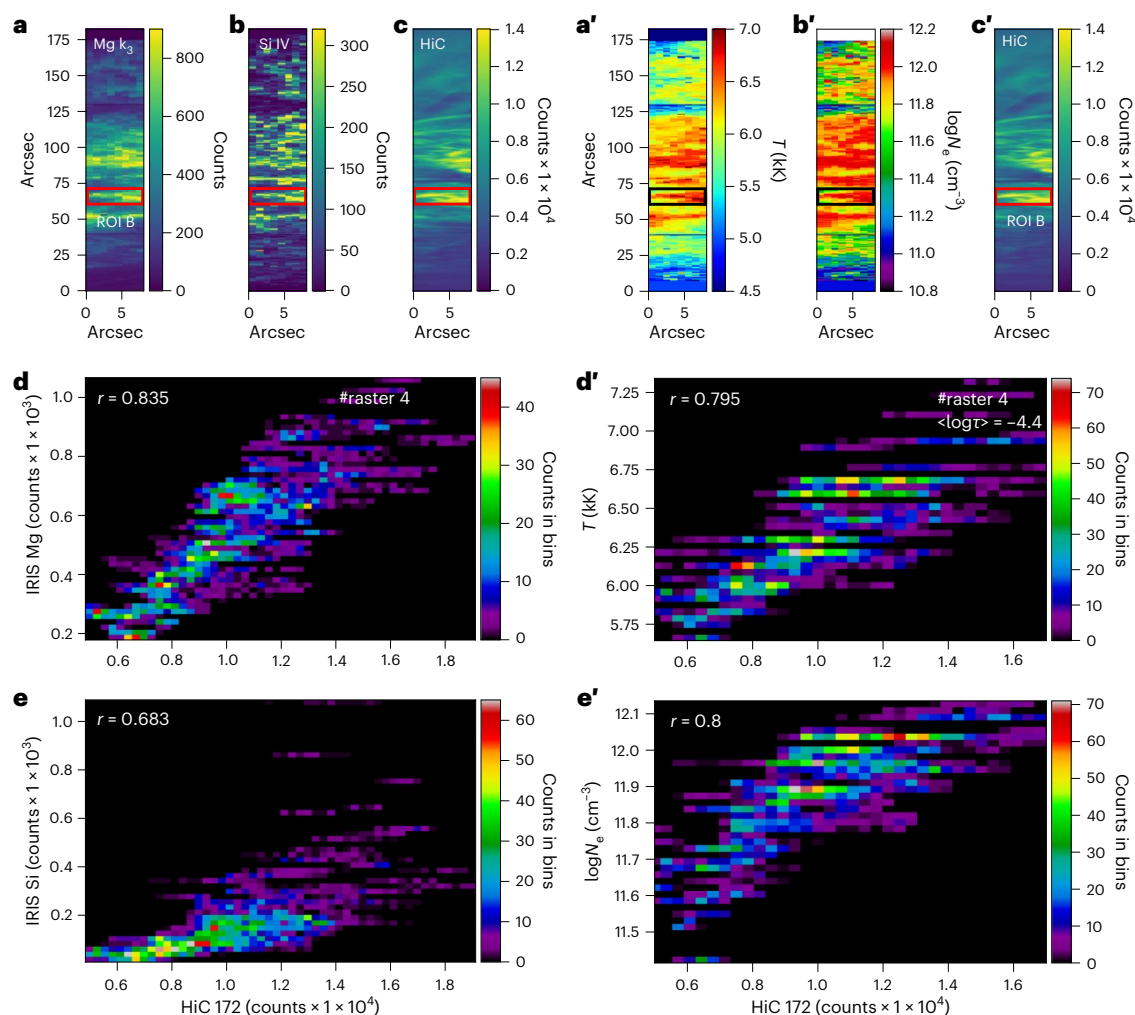


**Fig. 2 | Spatio-temporal correlation for the mossy plage region ROI-B.** **a–c.** The Mg II  $k_3$  (**a**), Si IV (**b**) and Hi-C (**c**) 172 Å intensity (counts) corresponding to the high-cadence raster (#4). The FOV under investigation is shown in red. **d,e.** The 2D density distribution functions between the Mg II  $k_3$  and Hi-C 172 Å (**d**) and the Si IV and Hi-C 172 Å (**e**) intensities. **a'–c'.** The  $T$  (**a'**) and  $N_e$  (**b'**) maps corresponding to the same time and FOV as **a** and **b** averaged

between  $\log\tau = [-4.6, -4.2]$ , and the Hi-C 172 Å (**c'**) as a reference. **d',e'.** The 2D density distribution functions between  $T$  and Hi-C 172 Å (**d'**), and  $N_e$  and Hi-C 172 Å (**e'**). The Pearson correlation coefficients ( $r$ ) are shown at the top left. An animation of this figure is available at [https://drive.google.com/drive/folders/1BV3mRUFSSur6k8yuRU-JdBewC\\_YNuWbP](https://drive.google.com/drive/folders/1BV3mRUFSSur6k8yuRU-JdBewC_YNuWbP).

## Results

### Chromosphere underneath the moss

Figure 1 shows the coronal and the chromospheric emission of the AR target 12712. The moss region, identified as a reticulated bright emission patch in Fig. 1a, is clearly seen to lie at the footpoints of the hotter ( $\sim 2\text{--}6$  MK; Fig. 1b and Methods) AR loops, typical of a moss<sup>4,5,7,18</sup>. IRIS co-observed the AR target, and we utilize the spectral information primarily in the Mg II h&k lines to explore the chromosphere underneath the moss that is characterized by regions of enhanced brightness in the Mg II  $k_3$  ( $h_3$ ) core. In Fig. 1c, such a region is indicated by the area bounded between  $X \approx 80\text{--}100''$  and  $Y \approx 40\text{--}100''$ , and it corresponds to a chromospheric plage. This observation is in agreement with Carlsson et al.<sup>6</sup>, who also reported that the Mg II k spectral line in plages shows little to no reversals of the upper chromospheric  $k_3$  core. Based on a semi-empirical radiative transfer approach, they argued that the enhanced core brightness in the plage represents conditions of hot and dense chromosphere, which causes the source function to remain strongly coupled with the local Planck function, thereby indicating locally strong heating.

Instead of an ad hoc forward modelling approach, we employ a state-of-the-art, simultaneous, multi-line inversion scheme based on

IRIS<sup>2</sup> (ref. 19) with six different spectral lines (including C II 1,335 Å; Methods). Figure 1d,e shows the plasma temperature ( $T$ ) and electron density ( $N_e$ ) maps derived from the inversion scheme, which upon inspection, immediately reveals clear evidence of hot and dense plasma in the regions associated with enhanced Mg II  $k_3$  radiation temperature ( $T_{\text{rad}}$ ; Fig. 1c). The radiation temperature is the temperature for which the Planck function reproduces the observed intensity at any given wavelength. Interestingly, the moss region (identified from Fig. 1a,b) shows stronger enhancement in the Mg II  $k_3$  radiation temperature that appears to be well correlated with stronger  $T$  and  $N_e$  values, which clearly suggests that the chromosphere underneath the moss has hotter and denser plasma associated with it. Including multiple atomic species in the inversion allows us to effectively constrain a wide range of solar atmosphere spanning the photosphere through the upper chromosphere<sup>20</sup>. This approach represents a major advancement since it enables a direct examination and correlation of the physical parameters of the plasma, instead of focusing on the ‘proxies’ of heating (as had been done in the past<sup>5,10</sup>).

A representative example of a Mg II h&k spectrum associated with a mossy plage pixel is shown in Fig. 1f. The spectrum shows little self-reversal in the  $k_3$  ( $h_3$ ) wavelength intensities, indicating a



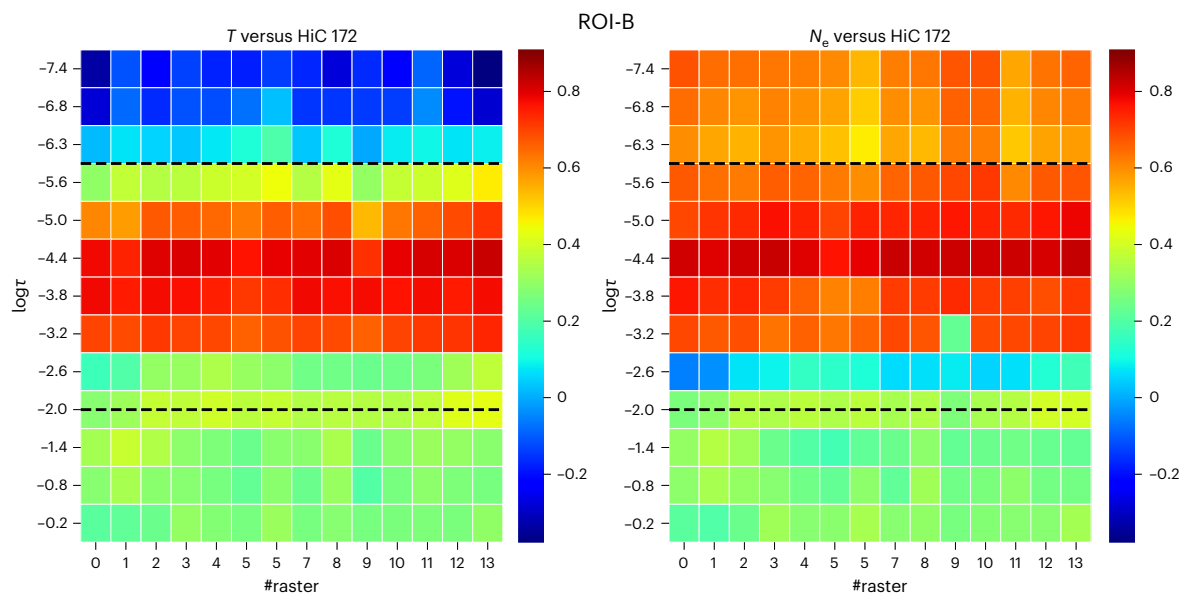


**Fig. 3 | Heatmaps showing the depth-dependent correlation for ROI-B.**

Pearson correlation coefficient ( $r$ , encoded in a rainbow colour scheme) as a function of depth in the solar atmosphere ( $\log\tau$ ,  $y$  axis) and time (#raster,  $x$  axis) for  $T$  versus Hi-C 172 Å (left) and  $N_e$  versus Hi-C 172 Å intensity (right).  $T$  and  $N_e$  are

derived from the multi-line inversions of the chromospheric IRIS data, and the region between the dashed lines in the two panels indicates the range of optical depths within which the inversions are sensitive (refer to main text). The number of rasters corresponds to the entire Hi-C 2.1 duration of ~5 min.

flat-topped (single-peaked<sup>6</sup>) profile unlike the quiet-Sun (QS) profiles, which show a distinct absorption in  $k_3$  ( $h_3$ ). Moreover, the overall  $T_{\text{rad}}$  and the width of the plage spectrum are substantially enhanced compared with the QS case, which is in agreement with earlier findings<sup>6</sup>. The synthetic spectra derived from inversion show good fit not only for the example shown in Fig. 1f but also for various other examples shown in Extended Data Figs. 1–3. Additionally, the C II lines, which were simultaneously inverted and fitted with the Mg II h&k, show good fits as well; this suggests that the derived physical parameters are well constrained at upper chromospheric heights. The inferred  $T$ , microturbulence and  $N_e$  as a function  $\log\tau$  ( $\tau$  being an ‘optical’ measure of depth in the solar atmosphere) corresponding to the plage and the QS spectra in Fig. 1f are shown in Fig. 1g–i. Interestingly, all three parameters show a clear enhancement centred around  $\log\tau = -4$  compared with the QS case, reinforcing that the chromosphere underneath the moss is hot and dense, and has substantial non-thermal velocities (of  $\sim 6 \text{ km s}^{-1}$ , here named as microturbulence). This pattern is consistently observed for a vast majority of the plage, including the examples shown in Extended Data Figs. 1–3. In addition, the temperature stratification shows a characteristic ‘step’ (around  $\log\tau = -4.5$ ), and the temperature minimum is pushed deeper into the solar atmosphere, which is critical (in combination with high density) in reproducing the flat-topped, single-peaked spectra.

### Correlation between chromospheric and coronal heating

The left and right panels of Fig. 2 show the spatio-temporal correlation analysis between the IRIS and the Hi-C intensities, and between the physical parameters derived from the IRIS<sup>2</sup> inversion and Hi-C intensity for a small field of view (FOV; of  $13 \times 7 \text{ arcsec}^2$ ) of the moss region marked as region of interest (ROI)-B. The analysis is derived from the high-cadence IRIS rasters (Methods) that overlap the moss region as shown in Fig. 1b. Visual inspection reveals that the intensity in ROI-B is well correlated among the Mg II  $k_3$ , Si IV and Hi-C channels. This is supported quantitatively in the form of the two-dimensional (2D) density distribution functions shown in Fig. 2d,e, where we see a tight correlation not only between Mg II  $k_3$  and Hi-C 172 Å intensities but also between Si IV and Hi-C 172 Å. The high values of Pearson coefficient ( $r$ ) in both cases are in direct contrast with earlier results

(such as refs. 4,5) where the authors failed to obtain a good correlation on (sub-)arcsecond scales. The correlation ( $r$ ) between Si IV and Hi-C 172 Å intensity is slightly worse and nonlinear compared with the chromospheric (Mg II  $k_3$ ) counterpart (also see Extended Data Figs. 4 and 5), possibly because TR Si IV is often impacted by shocks<sup>21</sup> and spicules<sup>5,9,22</sup> that affect its brightness variation more substantially compared with Mg II  $k_3$ . Nonetheless, the correlation coefficients obtained in this paper are substantially better than past findings, which implies a tight coupling in the heating of the solar atmosphere from the chromosphere to upper TR/lower corona around 1 MK.

The tight coupling in the moss intensity among the different channels directly translated to a strong visual correlation between the inferred physical parameters (Fig. 2, right), that is,  $T$  (Fig. 2a') and  $N_e$  (Fig. 2b') shown at  $\langle \log\tau \rangle = -4.4$ , where ‘ $\langle \rangle$ ’ represents an average of the physical parameter between  $\log\tau = [-4.6, -4.2]$ , with Hi-C 172 Å intensity (Fig. 2c'). In ROI-B, the enhanced Hi-C 172 Å intensity is clearly characterized by enhanced  $T$  and  $N_e$ . The range of the derived  $T$  and  $N_e$  is consistent with values that are typically observed in a chromospheric plage<sup>6,23</sup>. The 2D density distribution functions shown in Fig. 2d,e,d',e' further highlight the rigid coupling of the chromospheric and the upper TR/lower corona plasma in a moss. Moreover, the animation associated with Fig. 2 suggests that the correlation remains stable (and high) for the entire timeseries of the Hi-C data. Analysis of the spatio-temporal correlation analysis of other ROIs in the moss region (Extended Data Figs. 4 and 5) reveal similar results (with slightly different values of  $r$ ). This scenario does not appear to be compatible with the impact of non-thermal electrons, which causes a sudden temporal variability on timescales of  $\sim 15$ – $60 \text{ s}$  (refs. 13,14).

### Height dependence of the correlation

Although we found a good correlation between temperature, density (at mid-chromospheric heights) and Hi-C 172 Å intensity, an important question is: how deep in the solar atmosphere does the correlation still hold? The IRIS<sup>2</sup> database provides the derived thermodynamic parameters as a function of optical depth  $\tau$ . The latter is correlated with height, with smaller depths occurring at greater heights. We therefore studied the correlation over a range of heights in the solar atmosphere between  $\log\tau = [-7.6, 0]$ , that is, from the top of the chromosphere down to the

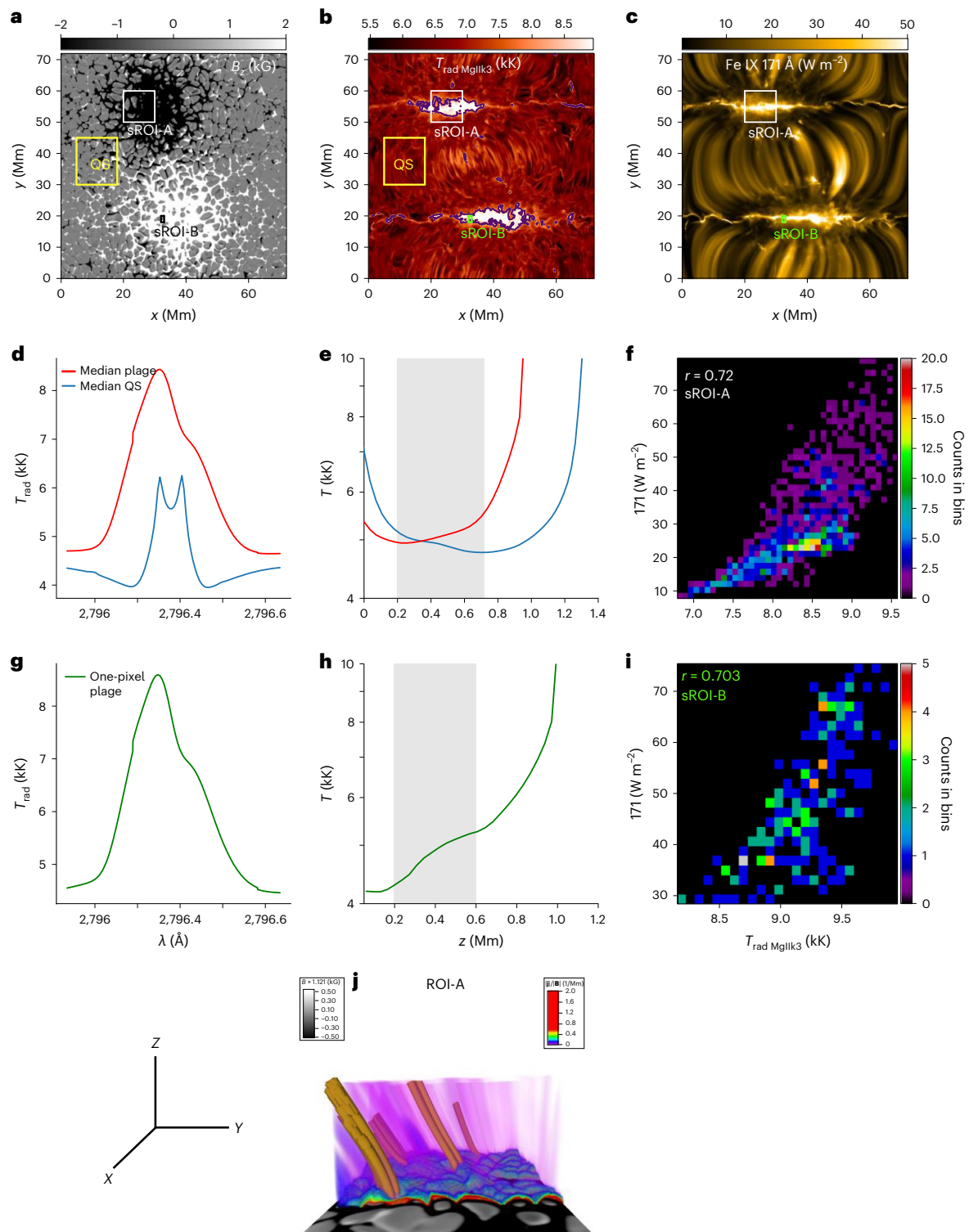


**Fig. 4 | Overview of the 3D numerical simulation of an AR plage.** **a**, Vertical magnetic field strength ( $B_z$ ) at  $z = 0$  Mm saturated between  $\pm 2$  kG. sROI-A and sROI-B cover an area of  $10 \times 10$  Mm $^2$  and  $1.5 \times 1.5$  Mm $^2$ , respectively, whereas the QS patch encloses an area of  $15 \times 15$  Mm $^2$ . **b, c**, Synthetic Mg II  $k_3$  and Fe IX 171 Å maps of the simulated plage. Purple contours in **b** indicate the regions of enhanced brightness corresponding to the moss emission in **c**. **d, e**, The synthetic median Mg II  $k$  spectra over the mossy pixels (red) within the purple contours in **b** and the QS patch (blue) (**d**), and the corresponding temperature stratification

(**e**). **g, h**, Illustrative examples of a synthetic Mg II  $k$  spectrum (**g**) and its ‘step-like’ temperature stratification (**h**; highlighted in grey) for a single mossy plage pixel in sROI-B. **f, i**, The 2D density distribution functions for sROI-A (**f**) and sROI-B (**i**). **j**, The visualization of the magnetic field lines (brownish yellow) and their associated current sheets ( $|\mathbf{j}|/|\mathbf{B}|$ ,  $\mathbf{j}$  being the current density) from the photosphere to the corona in sROI-A. The  $(x, y, z)$  dimensions of the ROI are  $13 \times 10 \times 5.5$  Mm $^3$ .

photosphere. This is represented in the form of a 2D heatmap in Fig. 3 that shows the Pearson  $r$  for ROI-B as a function of time (#raster) and optical depth ( $\log\tau$ ) for  $T$  (left) and  $N_e$  (right) versus Hi-C 172 Å intensity. The sensitivity of our inversions is predominantly limited between  $-6 \leq \log\tau \leq -2$  (due to the sensitivities of the different lines included in the inversion, see [Methods](#) and [ref. 20](#)). Interestingly, we find that there is a range of optical depths (within  $\log\tau = [-6, -2]$ ) for which  $r$  is rather high ( $\geq 0.6$ ) in both panels (Fig. 3). The temperature and density of the chromospheric plasma appear to be well correlated with the upper TR/lower coronal intensity of Hi-C 172 Å down to the temperature minimum ( $\log\tau \approx -3$ ) for all 14 rasters. The coupling immediately weakens deeper in the atmosphere (for  $\log\tau > -3$  in the photosphere), suggesting different physical conditions of the plasma. However, there is no doubt that hot and dense plasma dominates the lower to upper chromosphere underneath and is well correlated with upper TR/lower coronal moss locations. For heights above  $\log\tau = -6$ , the apparent absence (or presence) of correlation in Fig. 3 does not indicate a lack (or sufficiency) of coupling. It merely implies that the inferred values of  $T$  and  $N_e$  at these heights are ill constrained due to little or no sensitivity of the inversions. Analysis of the other ROIs reveals slightly different (and often lower peak) values of  $r$  (Extended Data Figs. 6 and 7), implying that different regions of the moss exhibit different behaviour at different epochs. Nonetheless, in both ROI-A and ROI-C, the correlation extends reasonably well down to at least  $\log\tau \approx -4$ , where the temperature is between 5 kK and 6 kK.

## Discussion

The tight correlation between the derived physical parameters with the Hi-C 172 Å intensity down to the temperature minimum strongly suggests the prevalence of a common heating mechanism. Thermal conduction, which obviously plays a role in the hot corona and upper TR<sup>10</sup>, is negligible at low temperatures in the lower chromosphere ( $\sim 6$  kK) and thus cannot explain the observed spatio-temporal correlation between low chromospheric and upper TR heating. Accelerated electron beams generated in coronal nanoflares can have an impact on heating the chromosphere<sup>24</sup>; however, due to their impulsive nature, such heating would show a high temporal variability<sup>13,14</sup>, which is not observed in this study.

We find that our observations show a striking correspondence with an advanced three-dimensional (3D) magnetohydrodynamic (MHD) numerical simulation of an AR plage (Fig. 4a–c). The numerical domain encompasses the convection zone, photosphere, chromosphere, TR and corona ([Methods](#)). Optically thin modelling of the coronal channels reveals the presence of moss-like emission patches in Fe IX 171 Å (Fig. 4c) that lie at the footpoints of hot loops visible in Fe XVI 335 Å (Extended Data Fig. 8). The synthetic Mg II  $k_3$  and 171 Å (Fig. 4b,c) intensity bear a close resemblance to observations where the moss coincides with enhanced  $k_3$  radiation, and the Mg II  $k$  spectra show single peaks (Fig. 4d,g). The temperature minimum is shifted deeper in the solar atmosphere for the moss pixels (Fig. 4d) with many showing characteristic ‘steps’ around low chromosphere at  $z = 0.4$  Mm (Fig. 4h), similar to Fig. 1f. Two-dimensional density distribution functions between 171 Å and  $k_3$  channels show a tight correlation with high values of Pearson  $r$  at both large (sROI-A; Fig. 4f) and small (sub-) arcsecond scales (sROI-B; Fig. 4i). The simulated scenario bears a close resemblance with observations, and a detailed analysis of the magnetic field topology reveals the presence of braiding in the field lines<sup>25</sup> deep in the atmosphere, which leads to the formation of current sheets (Fig. 4j). These sheets extend from the chromosphere (where they are stronger) to the corona, traversing several mega-metres and causing local heating in the mossy plage regions, in addition to the heating from the large downward thermal conductive flux from the overlying corona. Dissipation of the current sheets leads to strong heating of the plasma in the chromosphere and the upper TR/lower corona that explains the cause of the observed correlation. These types of

small-scale current sheets from braiding are more ubiquitous and very different from large-scale current sheets that form when newly emerging flux interacts with pre-existing fields and that have been implicated in local heating<sup>26</sup>. The current sheets in our simulation occur on small scales of several hundred kilometres that are at (and beyond) the limit of current observational capabilities<sup>27</sup>. High-resolution magnetic field measurements at multiple heights are needed to resolve some of these sheets. Future observations, for example, with 4 m DKIST<sup>28</sup>, may aid in this direction.

Furthermore, the nature of heating observed in the moss appears to be incompatible with current models of wave-based heating. Predicted heating rates from Alfvén wave turbulence models<sup>29,30</sup> are highly time varying because of the presence of high-frequency waves. This causes a lack of correlation between chromospheric and upper TR/lower coronal emission, in contrast to what we observe in this study. Future observations of longer duration with Solar Orbiter’s Extreme Ultraviolet Imager<sup>31</sup> instrument and the upcoming NASA Multi-slit Solar Explorer (MUSE) mission<sup>32</sup> will provide more detailed imaging and spectroscopy of a much wider variety of regions, and help determine how widespread this heating mechanism is in the solar atmosphere.

## Methods

### Observations

The Hi-C 2.1 sounding rocket mission was launched on 29 May 2018 at 18:54 UT from the White Sands Missile Range in New Mexico, United States. The target was AR 12712, and the instrument successfully acquired high spatial resolution (0.4”),  $2k \times 2k$  images with a 2 s exposure at a cadence of 4.4 s. The Solar Pointing and Aerobee Control System (SPARCS) maintained a constant target for the entire duration of the flight lasting 335 s. One of the major goals of this mission was to study the mass and energy coupling between the chromosphere and the corona in ARs. Consequently, the observations were recorded in the upper transition and lower coronal 172 Å passband (Fe IX/Fe X) that has a peak temperature sensitivity of about 1 MK. The passband is similar to the Atmospheric Imaging Assembly (AIA) 171 Å channel, except that Hi-C 2.1 recorded observations at roughly three times the spatial and temporal resolution of AIA, thereby allowing an unprecedented view of the million degree corona. The details of the instrument and its characterization can be found at [ref. 16](#).

The Hi-C 2.1 sounding rocket flight was also coordinated with IRIS that co-observed the AR target with multiple, co-temporal, high-cadence rasters centred around the moss brightenings (indicated by the dashed yellow lines in Fig. 1b). It ran in very large, sparse eight-step raster mode (OBS-3600104031) with a step size of 1” perpendicular to the slit and a raster cadence of 25 s covering a FOV of  $175'' \times 7''$  in the solar  $Y$  and  $X$  directions. A total of 256 rasters were obtained over a duration of 1 h 50 min, including the Hi-C flight duration of 5 min (equivalent to 14 rasters). In addition, IRIS also recorded several very large, dense 400 step rasters (OBS-3600010078) covering a FOV of  $141'' \times 174''$  co-spatially with Hi-C, but for roughly 1 h and 51 min (raster cadence) before and after the sounding rocket flight. The step size in this case was 0.35” perpendicular to the slit, while the step cadence was 16.7 s. The FOV of one such context raster is indicated in Fig. 1b, and the purpose of these rasters was to provide contextual information in and around the AR. Furthermore, IRIS recorded slit-jaw images (SJIs) in C II 1,330 Å, Si IV 1,400 Å, Mg II 2,796 Å and Mg continuum 2,832 Å channels sampling plasma from 6,000 K to  $\sim 100,000$  K. The cadence and the spatial sampling of these images are 13 s and 0.33”, respectively.

Finally, we also used observations in the Solar Dynamics Observatory<sup>33</sup>/AIA<sup>34</sup> 94 Å (Fe XVIII,  $\sim 6$  MK) and 335 Å (Fe XVI,  $\sim 2.5$  MK) passbands, solely for the purpose of visualizing the presence of hot AR loops above the moss brightenings seen in Hi-C 172 Å. This relationship is shown in the form of an RGB composite image in Fig. 1b.



## Data processing

The above sets of observations were precisely co-aligned using SolarSoftWare (SSW<sup>35</sup>) IDL routines including compensating for the roll angle (1.7°) between the IRIS and Hi-C observations. In particular, the IRIS SJI and Hi-C datasets were co-aligned through first a visual comparison and cross-correlation of Hi-C 172 Å and AIA 171 Å channels, followed by internally co-aligning the AIA 1,600 Å, 171 Å, 94 Å and 335 Å channels (this includes the 3 h cadence limb fitting), and finally by co-aligning the AIA 1,600 Å and IRIS 1,400 Å SJIs. The above steps resulted in a precise co-alignment between IRIS SJIs and the Hi-C 2.1 data (with an accuracy better than 0.5"), where the former was expanded<sup>36</sup>, rotated and spatio-temporally aligned to the latter. Extensive visualization with CRISPEX<sup>37</sup>, an IDL widget-based tool, showed good correspondence among the coordinated datasets.

For the spatio-temporal correlation analysis presented in the paper, synthetic sparse, eight-step Hi-C 172 Å rasters were generated that were spatially and temporally co-aligned with each of the IRIS rasters. This was done to ensure consistency between the IRIS and Hi-C observations, since the spectrograph slit takes time to 'build' the FOV whereas Hi-C observations over the whole FOV are instantaneous. Note that the derived parameters (for example, the intensity of Mg II  $k_3$ , Si IV,  $T$  and  $N_e$ ) from the IRIS rasters at original resolution were resampled to Hi-C 2.1 pixel scale (0.129") before generating the synthetic Hi-C rasters, which was done to not compromise the high spatial resolution of Hi-C. A standard single Gaussian fitting algorithm was applied to derive the Si IV peak intensity, while a double Gaussian approach (including one absorption and emission Gaussian as in ref. 38) was employed to fit the Mg II  $k$  spectra. This way, single-peaked profiles were easily fitted with the emission Gaussian whereas the remaining spectra with depressed cores were fitted with a superposition of a broad emission and narrower absorption Gaussian.

## IRIS<sup>2</sup> inversions

The inversions presented in this article were made using the IRIS<sup>2</sup> inversion framework. The core of this framework is a database created from the inversion of multi-line representative profiles (RPs) and their corresponding representative model atmospheres (RMAs).

This approach was first introduced by Sainz Dalda et al.<sup>19</sup>. There, the authors calculated the RPs of the Mg II h&k lines (including the Mg II UV lines located between the former ones) for a selection of IRIS datasets. The RPs are the average profile of those profiles belonging to a cluster. A cluster is calculated by using the  $k$ -means technique<sup>39,40</sup>. The profiles within a cluster share a similar shape; that is, the distribution of the intensity (spectral radiance) with respect to the wavelength is similar. Therefore, the physical conditions of the atmosphere where the radiation comes from are similar in the profiles within a cluster, and it is encoded in the RP of the cluster. The database was created considering a large variety of RPs belonging to different solar features with different observational setups, for example, exposure time, location on the solar disk, raster steps, etc. These RPs were inverted by the state-of-the-art STockholm Inversion Code (STiC<sup>41</sup>), which considers non-LTE radiative transfer and the partial frequency distribution (PRD) of the scattered photons. This code is capable of inverting simultaneously several spectral lines from different atomic species, in both non-LTE and LTE. STiC solves the radiative transfer problem to synthesize the spectral lines in the RP, and in an iterative process that slightly changes the physical parameters of an initial guess model, looks for the best possible fit between the synthetic profile and the observed RP. This process is repeated until convergence under a given limit or computational constraint. As a result of the inversion, STiC provides a synthetic RP that best fits the observed RP, and the RMA that reproduces that synthetic RP. An RMA consists of thermodynamic parameters (for example,  $T$ ,  $N_e$ , LOS velocity and microturbulence) as a function of optical depth ( $\tau$ ). For a given observed Mg II h&k profile in an IRIS observation, IRIS<sup>2</sup> looks for the closest synthetic RP in their database that fits that observed

profile and associates the RMA to the location in the data set where the observed profile was recorded. This method speeds up the inversion of a data set by a factor of  $10^5$ – $10^6$ .

In this paper, we use an extended version of the IRIS<sup>2</sup> method. Sainz Dalda et al. (2022)<sup>20</sup> use the same method and calculate the RPs for multi-line profiles containing the C II lines, the Mg II h&k lines, the three lines of the Mg II UV triplet and six photospheric lines located around the Mg II h&k spectral range. Thus, a multi-line RP is simultaneously inverted by STiC providing an RMA, for which the thermodynamic parameters are constrained from the top of the chromosphere to the bottom of the photosphere (see ref. 20 for more details). Note that, because we are considering simultaneously several lines that are sensitive to variations of the thermodynamics in the same region of the solar atmosphere, the  $T$  and the non-thermal contribution to the profile (microturbulence) are better constrained than in the case that only considers one spectral line, which is the case for both the chromosphere and the low photosphere. Thus, this set of RPs and RMAs is probably the best-constrained, comprehensive database of thermodynamics models of the low solar atmosphere.

For this paper, IRIS<sup>2</sup> looked for the closest RP in the database considering only the lines available in our data sets, which are the C II lines, the Mg II h&k lines, the three Mg II UV triplet lines and the photospheric Ni I at 2,815.18 Å line. Extended Data Figs. 1–3 show the observed lines in the chromosphere (dotted red line) and their fits (black). Thus, although the RMA provided by IRIS<sup>2</sup> contains information that was obtained from inverting six photospheric lines, the information presented in this paper comes from fitting only one photospheric line. Therefore, the values in the region  $\log \tau = [-2, 0]$  must be considered with caution. We are, however, very confident in the values obtained in the chromosphere, especially between  $\log \tau = [-6, -2]$ , since that information comes from the unique simultaneous inversion of six chromospheric lines, which provide model atmospheres with excellent constraint in these heights, and the photospheric Ni I at 2,815.18 Å line. Although this method reproduces most of the characteristics of the Mg II spectral lines, in some cases, for example, in Extended Data Fig. 2, there is a discrepancy between the fitted and the observed spectra around the  $k_3$  ( $h_3$ ) region that can be attributed to the lack of similar profiles in the IRIS<sup>2</sup> database.

## Numerical simulation

The 3D simulation of the plage-like region was performed in a computational box with dimensions of  $72 \times 72 \times 61$  Mm spanning from 8.5 Mm below the photosphere to 52.5 Mm above it. The resolution of this box is moderate: 100 km in the horizontal directions and [20, 100] km in the vertical direction, depending on location in the atmosphere; in the photosphere, chromosphere and TR, the vertical resolution is on the order of 20 km. The model calculations are run with the Bifrost radiative-MHD code<sup>42</sup>, which includes optically thick radiative transfer in the photosphere and lower chromosphere, radiative losses in the mid- and upper chromosphere and optically thin radiative losses in the corona. The radiative heating and cooling of the chromosphere and corona are calculated using tables derived by ref. 43 in which neutral hydrogen lines and the Lyman continuum, the H and K and infra-red triplet lines of singly ionized calcium and the h and k lines of singly ionized magnesium are written as a product of an optically thin emission (dependent on temperature), an escape probability (dependent on column mass) and an ionization fraction (dependent on temperature). Spitzer thermal conduction along the magnetic field is handled by a multi-grid method (or alternately by the hyperbolic method developed by ref. 44) to maintain time steps at a reasonable level. The upper boundary at  $z = 52$  Mm above the photosphere is set to be transparent by using characteristic equations as described in ref. 42. The lower boundary, some 8.5 Mm below the photosphere, sets the entropy of inflowing material such that the effective temperature of the model is close to solar conditions,

while other variables such as density, velocities and magnetic field are extrapolated out of the box on the basis of their values at the boundary. In the horizontal direction, the boundaries are periodic. The code is kept stable by using hyperdiffusivities, which are again described in ref. 42; this gives heating of the plasma where magnetic gradients are large through a numerical Joule heating term. In addition, such reconnection sites lead to an acceleration of the plasma that is thermalized by the (hyperdiffusive) viscosity. Both terms lead to the energization of the chromospheric and coronal plasma in the vicinity of the current sheets formed by tangential discontinuities in the magnetic field.

To initialize the model, two circular patches of strong but opposite polarity magnetic flux (at 8.5 Mm below the photosphere) were used to generate a potential field covering the entire computational box. The positive polarity patch started with a diameter of 20 Mm, while the negative polarity patch had a diameter of 15 Mm at the bottom boundary. The total flux in each patch was set to be opposite but equal, while a small positive (vertical) flux of a few Gauss was added to the entire area of the simulation. This field geometry was inserted into a relaxed convective atmosphere after which the field and atmosphere were allowed to relax together. At the time of the snapshot, some 20 min after the initial snapshot, the photosphere in the strong field regions has become quite cold (and darker than the surrounding atmosphere) while the chromosphere and corona are hot and bright (Fig. 4 and Extended Data Fig. 8).

To compute the Mg II lines, we used the RH1.5D code<sup>45,46</sup>. This code includes detailed radiative physics including polarized transfer and PRD, but at the cost of only being used for 1.5D (column-by-column) computations, and thus ignores the 3D effects of lateral transport of radiation. Three-dimensional effects can play an important role in modelling the Mg II lines<sup>17</sup>, especially in the line cores. However, in regions where the temperature and the density of the plasma are enhanced (such as in the mossy plage), 3D effects can be minimal due to lower scattering of photons. Moreover, the lower time complexity of the 1.5D approach far outweighs its limitations. The calculations are carried out in non-LTE assuming PRD.

The emission of optically thin TR and coronal lines, including the Fe IX 17.1 nm and Fe XVI 33.5 nm lines, is calculated using contribution functions  $G(T, N_e)$  from the CHIANTI<sup>47</sup> database package. These contribution functions are integrated along the line of sight using the local values of the electron density  $N_e$ , the temperature  $T$ , and the velocity along the line of sight  $u_z$  at several frequencies covering the emitting ions line profile. These calculations are done on GPUs using a Cuda code developed by Juan Martinez-Sykora.

## Data availability

The Hi-C flight 2.1 datasets are publicly available through the Virtual Solar Observatory at <https://msfc.virtualsolar.org/Hi-C2.1/>, and the coordinated high-cadence IRIS and AIA datasets are available at [https://msfc.virtualsolar.org/Hi-C2.1/coordinated\\_observations/](https://msfc.virtualsolar.org/Hi-C2.1/coordinated_observations/). The 3D MHD simulation snapshot analysed during the current study is available from the corresponding author upon reasonable request.

## Code availability

The IRIS<sup>2</sup> code, which is central to chromospheric inversions, is available via SolarSoftWare package of Interactive Data Language (IDL) and is extensively described in <https://iris.lmsal.com/iris2/>. The RH1.5D forward modelling code is publicly available at <https://github.com/ITA-Solar/rh>.

## References

- Schrijver, C. J. Magnetic structure in cool stars. XI. Relations between radiative fluxes measuring stellar activity, and evidence for two components in stellar chromospheres. *Astron. Astrophys.* **172**, 111–123 (1987).
- Ayres, T. R. In the trenches of the solar–stellar connection. I. Ultraviolet and X-ray flux–flux correlations across the activity cycles of the Sun and Alpha Centauri AB. *Astrophys. J. Suppl.* **250**, 16 (2020).
- Ayres, T. R. In the trenches of the solar–stellar connection. II. Extreme ultraviolet flux–flux correlations across solar cycle 24. *Astrophys. J.* **908**, 205 (2021).
- De Pontieu, B., Berger, T. E., Schrijver, C. J. & Title, A. M. Dynamics of transition region ‘Moss’ at high time resolution. *Sol. Phys.* **190**, 419–435 (1999).
- De Pontieu, B., Tarbell, T. & Erdélyi, R. Correlations on arcsecond scales between chromospheric and transition region emission in active regions. *Astrophys. J.* **590**, 502–518 (2003).
- Carlsson, M., Leenaarts, J. & De Pontieu, B. What do IRIS observations of Mg II k tell us about the solar plage chromosphere? *Astrophys. J. Lett.* **809**, L30 (2015).
- Berger, T. E. et al. What is moss? *Sol. Phys.* **190**, 409–418 (1999).
- Keller, C. U., Schüssler, M., Vögler, A. & Zakharov, V. On the origin of solar faculae. *Astrophys. J. Lett.* **607**, L59–L62 (2004).
- De Pontieu, B. et al. Rapid temporal variability of faculae: high-resolution observations and modeling. *Astrophys. J.* **646**, 1405–1420 (2006).
- Vourlidas, A., Klimchuk, J. A., Korendyke, C. M., Tarbell, T. D. & Handy, B. N. On the correlation between coronal and lower transition region structures at arcsecond scales. *Astrophys. J.* **563**, 374–380 (2001).
- Kobayashi, K. et al. The High-Resolution Coronal Imager (Hi-C). *Sol. Phys.* **289**, 4393–4412 (2014).
- De Pontieu, B. et al. The Interface Region Imaging Spectrograph (IRIS). *Sol. Phys.* **289**, 2733–2779 (2014).
- Testa, P. et al. Observing coronal nanoflares in active region moss. *Astrophys. J. Lett.* **770**, L1 (2013).
- Testa, P., Polito, V. & De Pontieu, B. IRIS observations of short-term variability in moss associated with transient hot coronal loops. *Astrophys. J.* **889**, 124 (2020).
- Parker, E. N. Nanoflares and the solar X-ray corona. *Astrophys. J.* **330**, 474 (1988).
- Rachmeler, L. A. et al. The High-Resolution Coronal Imager, Flight 2.1. *Sol. Phys.* **294**, 174 (2019).
- Leenaarts, J., Pereira, T. M. D., Carlsson, M., Uitenbroek, H. & De Pontieu, B. The formation of IRIS diagnostics. II. The formation of the Mg II h&k lines in the solar atmosphere. *Astrophys. J.* **772**, 90 (2013).
- Tripathi, D., Mason, H. E., Del Zanna, G. & Young, P. R. Active region moss. Basic physical parameters and their temporal variation. *Astron. Astrophys.* **518**, A42 (2010).
- Sainz Dalda, A., de la Cruz Rodríguez, J., De Pontieu, B. & Gošić, M. Recovering thermodynamics from spectral profiles observed by IRIS: a machine and deep learning approach. *Astrophys. J. Lett.* **875**, L18 (2019).
- Sainz Dalda, A., Agrawal, A., De Pontieu, B. & Gosic, M. IRIS<sup>2</sup>: a comprehensive database of stratified thermodynamic models in the low solar atmosphere. *Astrophys. J. Suppl. Ser.* **271**, 24 (2024).
- Martinez-Sykora, J. et al. Internetwork chromospheric bright grains observed with IRIS and SST. *Astrophys. J.* **803**, 44 (2015).
- Bose, S. et al. Evidence of the multi-thermal nature of spicular downflows. Impact on solar atmospheric heating. *Astron. Astrophys.* **654**, A51 (2021).
- da Silva Santos, J. M. et al. The multi-thermal chromosphere. Inversions of ALMA and IRIS data. *Astron. Astrophys.* **634**, A56 (2020).
- Frogner, L., Gudiksen, B. V. & Bakke, H. Accelerated particle beams in a 3D simulation of the quiet Sun. *Astron. Astrophys.* **643**, A27 (2020).



25. Parker, E. N. Magnetic neutral sheets in evolving fields. I—General theory. *Astrophys. J.* **264**, 635–647 (1983).
26. da Silva Santos, J. M. et al. Heating of the solar chromosphere through current dissipation. *Astron. Astrophys.* **661**, A59 (2022).
27. Anan, T. et al. Measurements of photospheric and chromospheric magnetic field structures associated with chromospheric heating over a solar plage region. *Astrophys. J.* **921**, 39 (2021).
28. Rimmele, T. R. et al. The Daniel K. Inouye Solar Telescope—observatory overview. *Sol. Phys.* **295**, 172 (2020).
29. van Ballegooyen, A. A., Asgari-Targhi, M. & Berger, M. A. On the relationship between photospheric footpoint motions and coronal heating in solar active regions. *Astrophys. J.* **787**, 87 (2014).
30. van Ballegooyen, A. A., Asgari-Targhi, M. & Voss, A. The heating of solar coronal loops by Alfvén wave turbulence. *Astrophys. J.* **849**, 46 (2017).
31. Rochus, P. et al. The Solar Orbiter EUV instrument: the extreme ultraviolet imager. *Astron. Astrophys.* **642**, A8 (2020).
32. De Pontieu, B. et al. The multi-slit approach to coronal spectroscopy with the Multi-slit Solar Explorer (MUSE). *Astrophys. J.* **888**, 3 (2020).
33. Pesnell, W. D., Thompson, B. J. & Chamberlin, P. C. The Solar Dynamics Observatory (SDO). *Sol. Phys.* **275**, 3–15 (2012).
34. Lemen, J. R. et al. The Atmospheric Imaging Assembly (AIA) on the Solar Dynamics Observatory (SDO). *Sol. Phys.* **275**, 17–40 (2012).
35. Freeland, S. L. & Handy, B. N. Data analysis with the SolarSoft system. *Sol. Phys.* **182**, 497–500 (1998).
36. Park, S. K. & Schowengerdt, R. A. Image reconstruction by parametric cubic convolution. *Comput. Vis. Graph. Image Process.* **23**, 258–272 (1983).
37. Vissers, G. & Rouppe van der Voort, L. Flocculent flows in the chromospheric canopy of a sunspot. *Astrophys. J.* **750**, 22 (2012).
38. Schmit, D. et al. Observed variability of the solar Mg II h spectral line. *Astrophys. J.* **811**, 127 (2015).
39. Steinhaus, H. Sur la division des corps matériels en parties. *Bull. Acad. Pol. Sci. Cl. III* **4**, 801–804 (1957).
40. MacQueen, J. Classification and analysis of multivariate observations. In *5th Berkeley Symp. Math. Statist. Probability* 281–297 (University of California Press, 1967).
41. de la Cruz Rodríguez, J., Leenaarts, J., Danilovic, S. & Uitenbroek, H. STiC: a multiatom non-LTE PRD inversion code for full-Stokes solar observations. *Astron. Astrophys.* **623**, A74 (2019).
42. Gudiksen, B. V. et al. The stellar atmosphere simulation code Bifrost. Code description and validation. *Astron. Astrophys.* **531**, A154 (2011).
43. Carlsson, M. & Leenaarts, J. Approximations for radiative cooling and heating in the solar chromosphere. *Astron. Astrophys.* **539**, A39 (2012).
44. Rempel, M. Small-scale dynamo simulations: magnetic field amplification in exploding granules and the role of deep and shallow recirculation. *Astrophys. J.* **859**, 161 (2018).
45. Uitenbroek, H. Multilevel radiative transfer with partial frequency redistribution. *Astrophys. J.* **557**, 389–398 (2001).
46. Pereira, T. M. D. & Uitenbroek, H. RH 1.5D: a massively parallel code for multi-level radiative transfer with partial frequency redistribution and Zeeman polarisation. *Astron. Astrophys.* **574**, A3 (2015).
47. Del Zanna, G., Dere, K. P., Young, P. R., Landi, E. & Mason, H. E. CHIANTI—an atomic database for emission lines. Version 8. *Astron. Astrophys.* **582**, A56 (2015).

## Acknowledgements

S.B., V.H., A.S.D. and B.D.P. gratefully acknowledge support from NASA contract NNG09FA40C (IRIS). B.D.P. was also supported by grant NNM16AA10P (Hi-C). We acknowledge the High-Resolution Coronal Imager (Hi-C 2.1) instrument team for making the second re-flight data available under NASA proposal 17-HTIDS17\_2-003. MSFC/NASA led the mission with partners including the Smithsonian Astrophysical Observatory, the University of Central Lancashire and the Lockheed Martin Solar and Astrophysics Laboratory. Hi-C 2.1 was launched out of the White Sands Missile Range on 2018 May 29. IRIS is a NASA small explorer mission developed and operated by LMSAL with mission operations executed at NASA Ames Research Center and major contributions to downlink communications funded by ESA and the Norwegian Space Centre. The 3D visualization of the numerical simulation was carried out using VAPOR, a product of the Computational Information Systems Laboratory at the National Center for Atmospheric Research.

## Author contributions

S.B. was responsible for most of the analysis and writing of the paper. B.D.P. designed the study and performed initial analysis and final editing. V.H. performed the numerical simulations, and calculation of synthetic observables, and assisted with the analysis of the simulations. A.S.D. performed the inversions. S.S. and A.W. designed, built and operated the Hi-C sounding rocket experiment. All authors reviewed the paper.

## Competing interests

The authors declare no competing interests.

## Additional information

**Extended data** is available for this paper at <https://doi.org/10.1038/s41550-024-02241-8>.

**Correspondence and requests for materials** should be addressed to Souvik Bose.

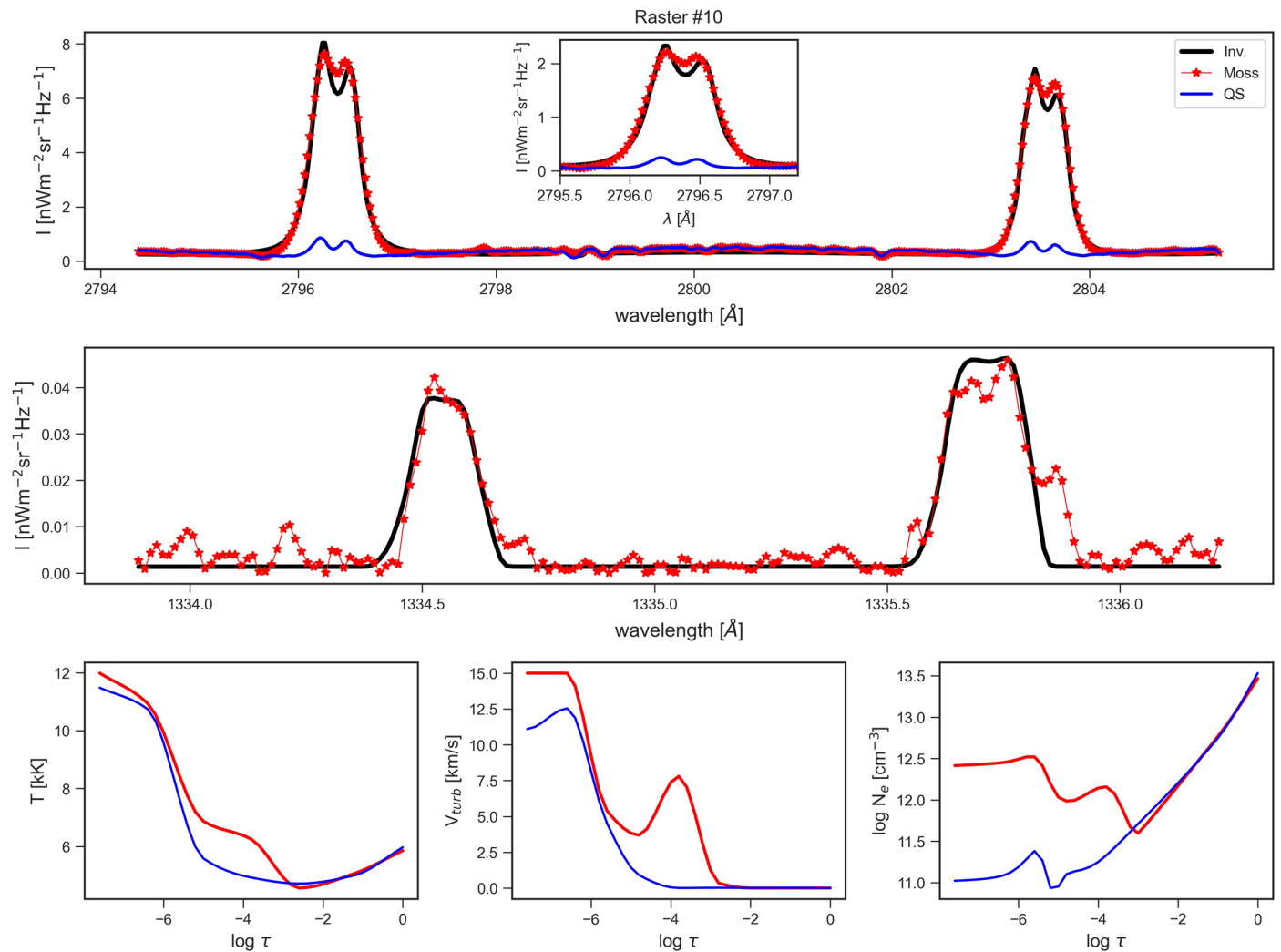
**Peer review information** *Nature Astronomy* thanks the anonymous reviewers for their contribution to the peer review of this work.

**Reprints and permissions information** is available at [www.nature.com/reprints](http://www.nature.com/reprints).

**Publisher's note** Springer Nature remains neutral with regard to jurisdictional claims in published maps and institutional affiliations.

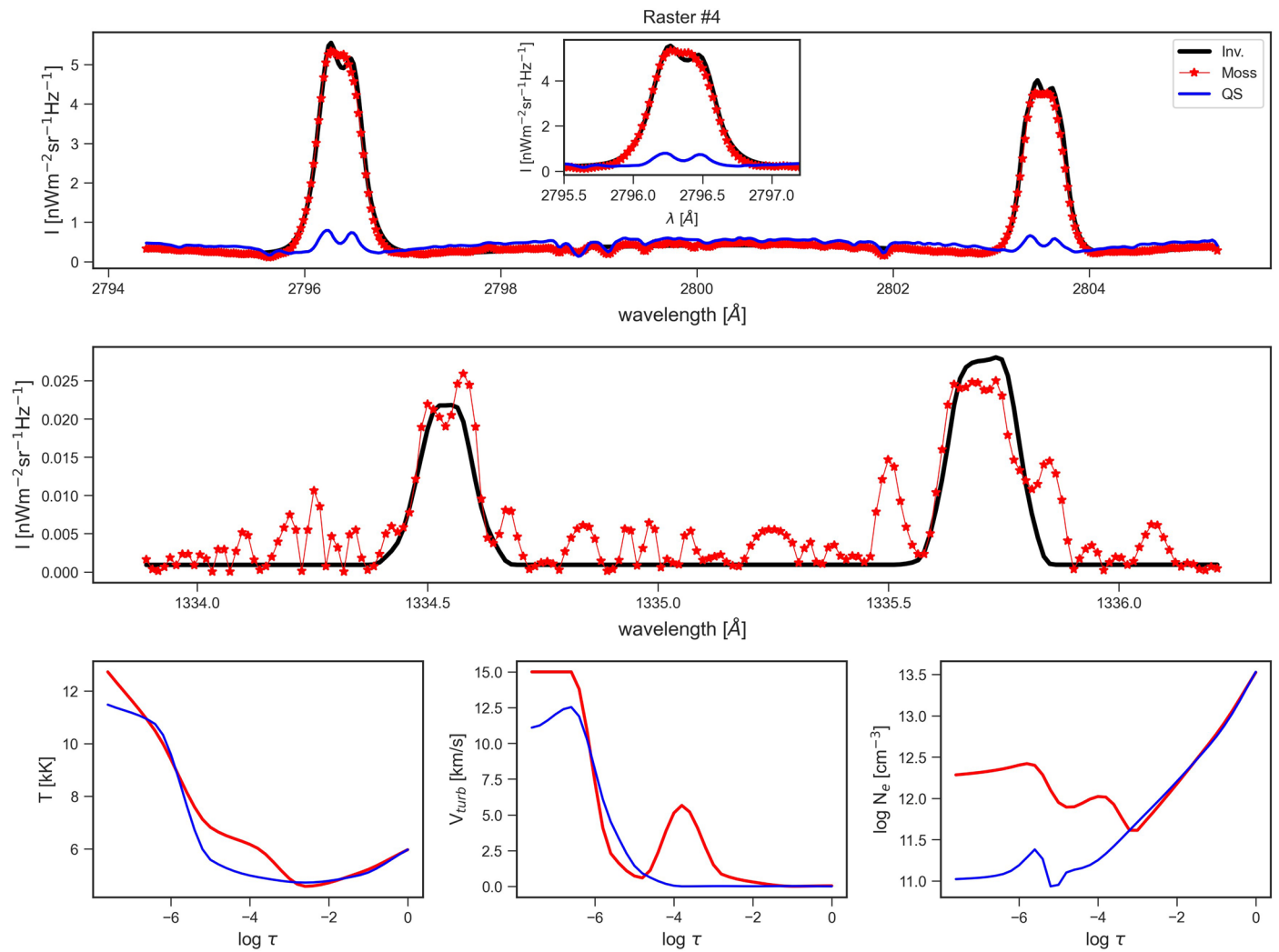
**Open Access** This article is licensed under a Creative Commons Attribution 4.0 International License, which permits use, sharing, adaptation, distribution and reproduction in any medium or format, as long as you give appropriate credit to the original author(s) and the source, provide a link to the Creative Commons licence, and indicate if changes were made. The images or other third party material in this article are included in the article's Creative Commons licence, unless indicated otherwise in a credit line to the material. If material is not included in the article's Creative Commons licence and your intended use is not permitted by statutory regulation or exceeds the permitted use, you will need to obtain permission directly from the copyright holder. To view a copy of this licence, visit <http://creativecommons.org/licenses/by/4.0/>.

© The Author(s) 2024



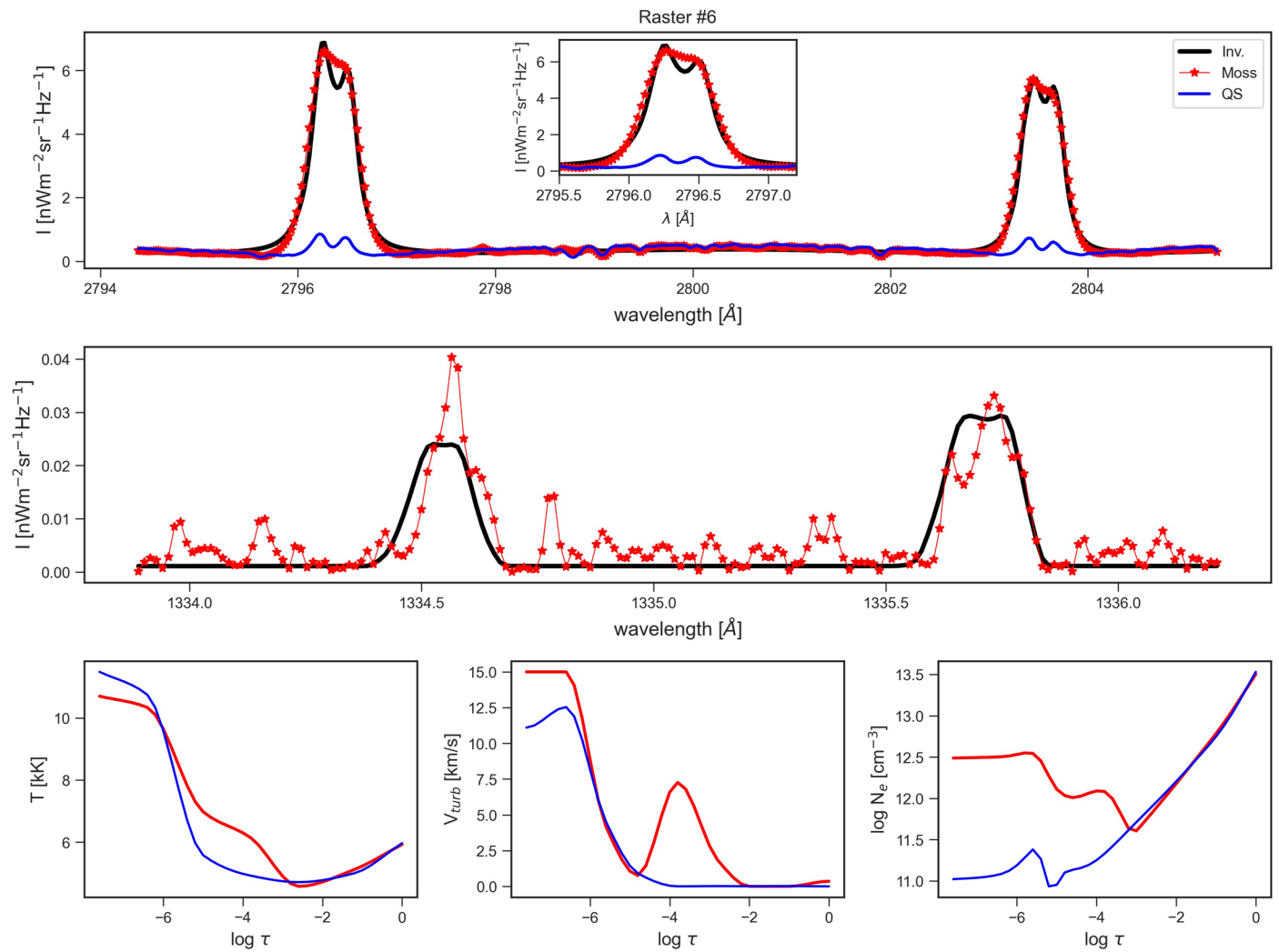
**Extended Data Fig. 1 | Comparison of the observed and fitted Mg II h&k (top row) and C II 1335 Å (middle row) spectra for a mossy plage pixel from IRIS raster #4. The derived stratification of  $T$ , microturbulent velocity ( $V_{\text{turb}}$ ), and**

$N_e$  and their comparison with a typical QS atmosphere is shown in the bottom row. The intensity variation between the two C II 1335 Å lines in the middle row is attributed to noise and hence should not be compared to judge the fitting.

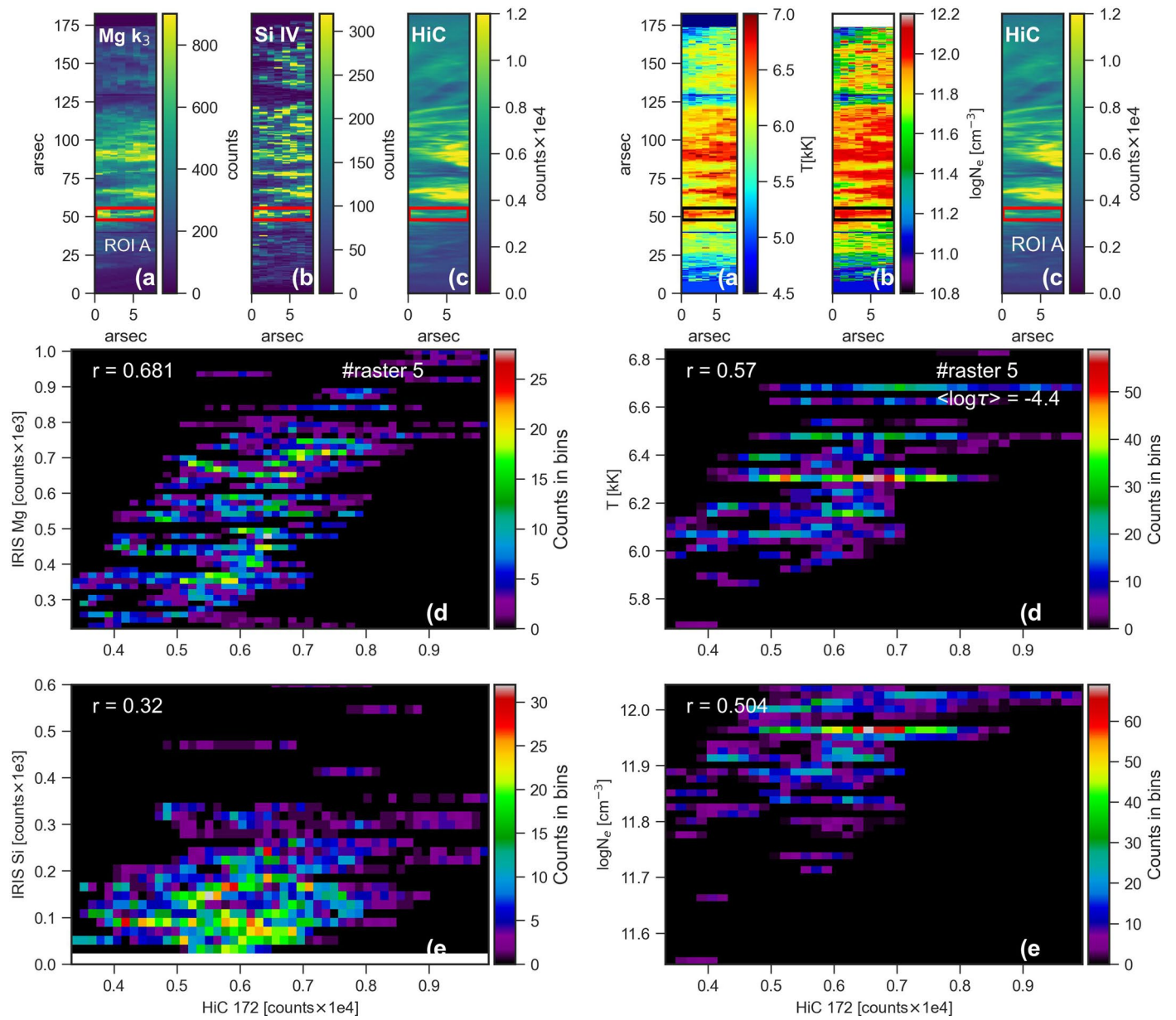


**Extended Data Fig. 2 | Comparison of the observed and fitted Mg II h&k (top row) and C II 1335  $\text{\AA}$  (middle row) spectra for a mossy plage pixel.** Second example from IRIS raster #6 showing the fits between the observed and the synthetic spectra for a pixel in a moss region, in the same format as Extended Data Fig. 1.

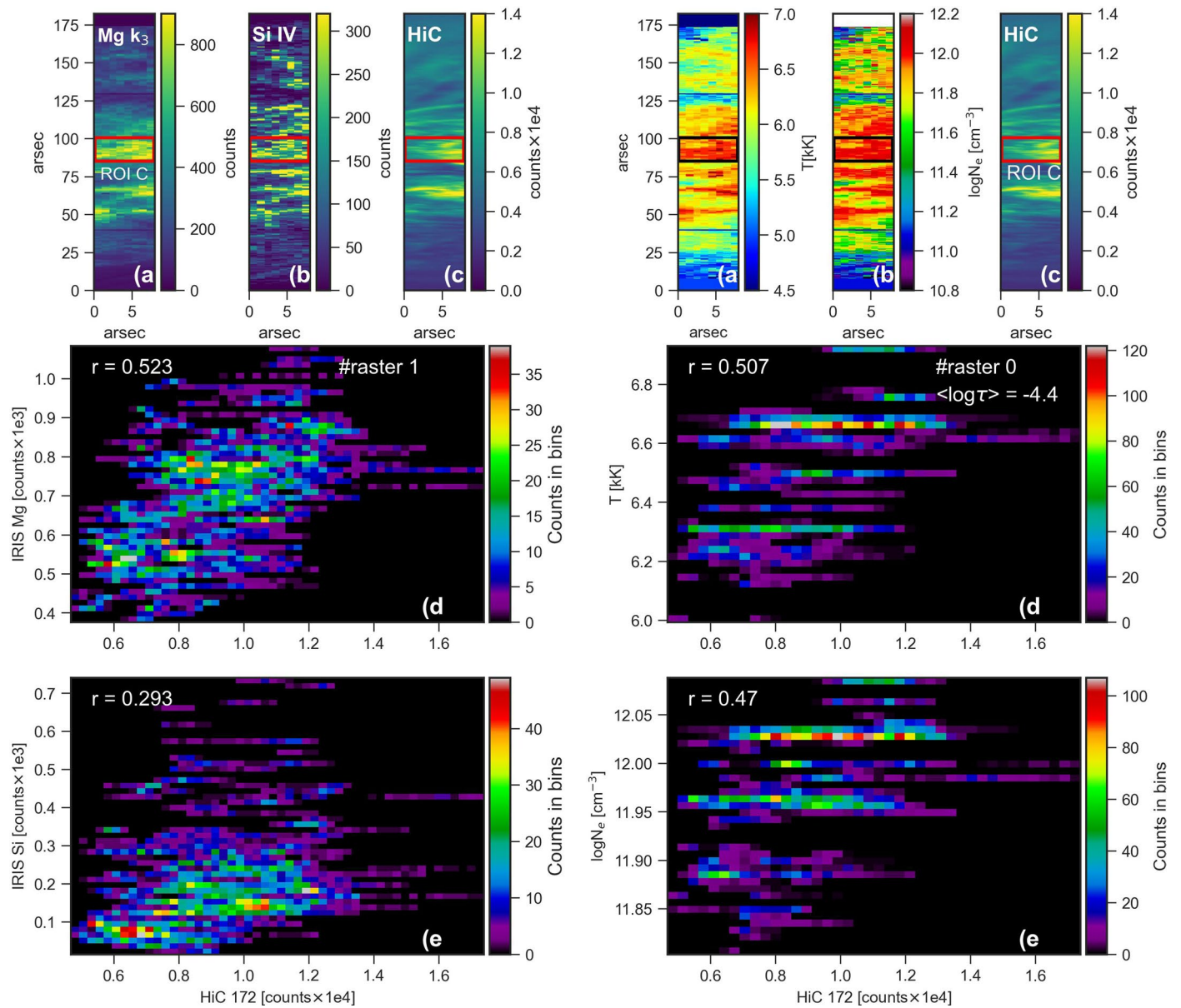




**Extended Data Fig. 3 | Comparison of the observed and fitted Mg II h&k (top row) and C II 1335  $\text{\AA}$  (middle row) spectra for a mossy plage pixel.** Third example from IRIS raster #10 showing the fits between the observed and the synthetic spectra for a pixel in a moss region in the same format as Extended Data Fig. 1.

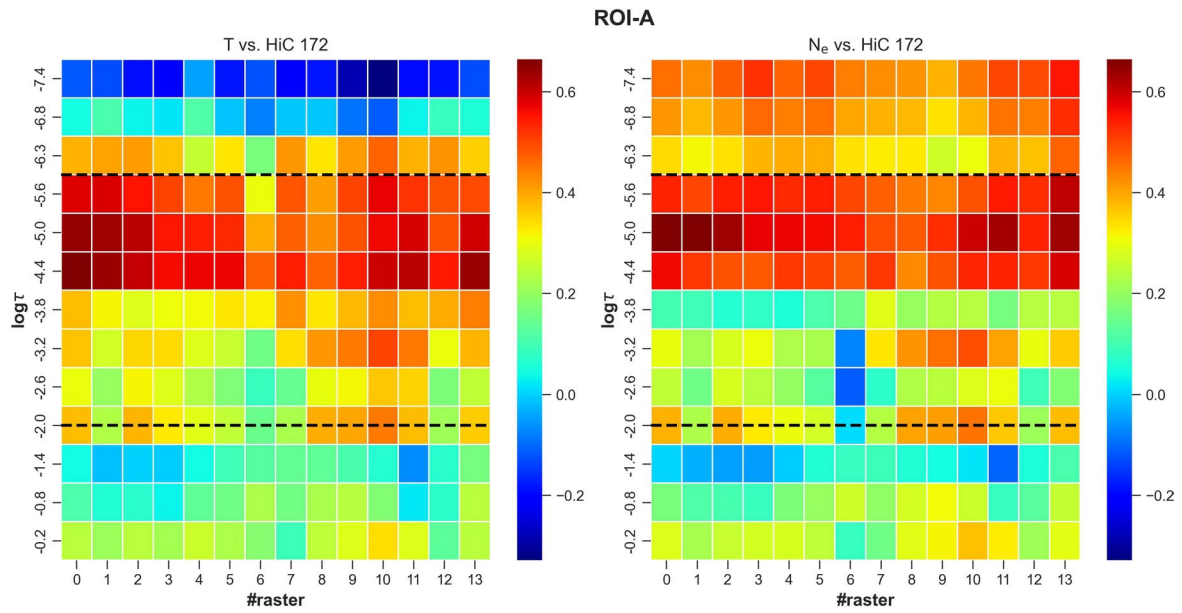


**Extended Data Fig. 4 | Spatio-temporal correlation for the mossy plage region ROI-A.** Same as Fig. 2 but for ROI-A.

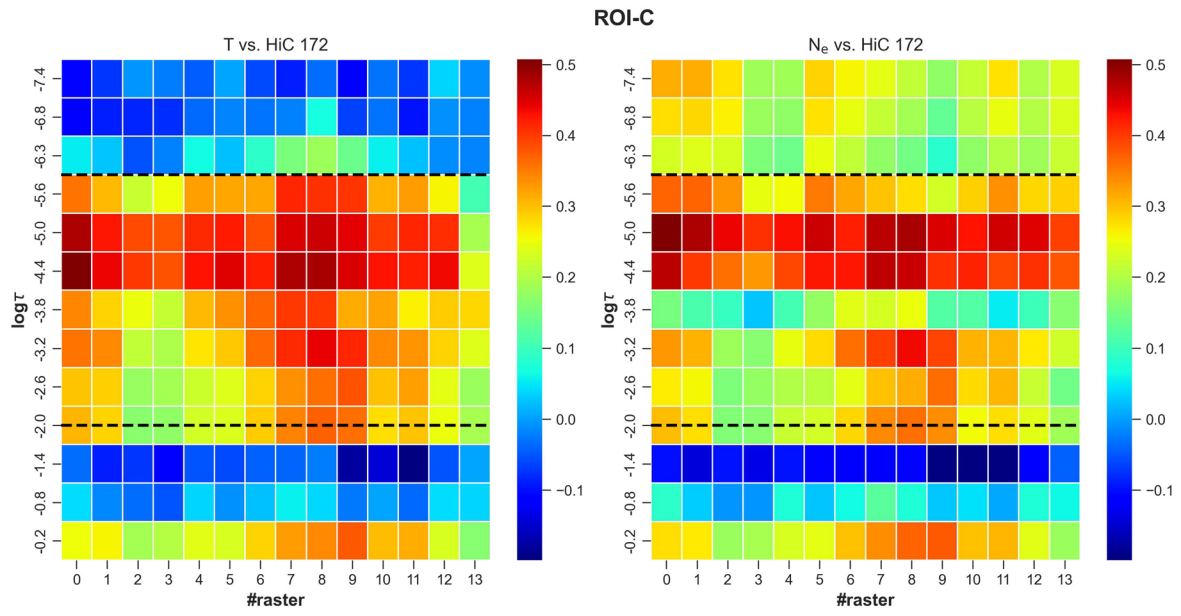


**Extended Data Fig. 5** | Spatio-temporal correlation for the mossy plage region ROI-C. Same as Fig. 2 but for ROI-C.

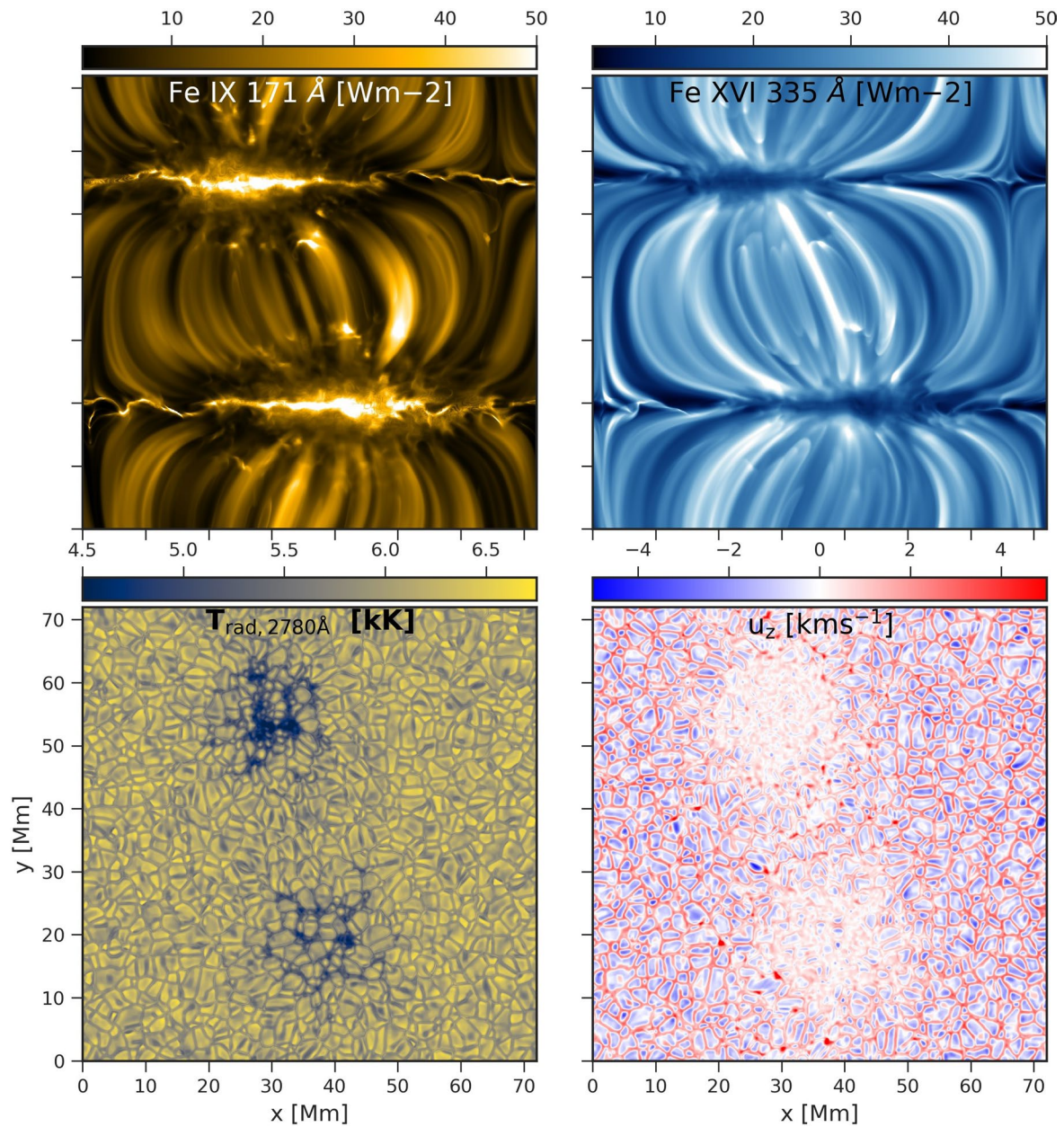




**Extended Data Fig. 6 | Heatmaps showing the depth dependent correlation for ROI-A.** Heatmap showing the depth dependent correlation coefficients for ROI-A in the same format as Fig. 3.



**Extended Data Fig. 7 | Heatmaps showing the depth dependent correlation for ROI-C.** Heatmap showing the depth dependent correlation coefficients for ROI-C in the same format as Fig. 3.



**Extended Data Fig. 8 | Coronal and photospheric scenery of the 3D MHD plage simulation.** Top left: Synthetic Fe IX 171 Å emission showing bright, reticulated moss patches. Top right: Synthetic Fe XVI 335 Å emission showing

hot (2.5 MK) loops overlying the moss. Lower left: Synthetic photospheric radiation temperature at 2780 Å at  $z=0$  Mm. Lower right: Vertical velocity ( $u_z$ ) map at  $z=0$  Mm.